

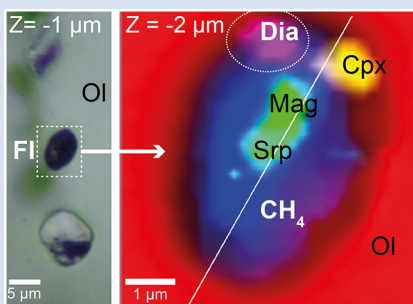
# Diamond forms during low pressure serpentinisation of oceanic lithosphere

N. Pujol-Solà<sup>1\*</sup>, A. Garcia-Casco<sup>2,3</sup>, J.A. Proenza<sup>1,4</sup>, J.M. González-Jiménez<sup>2</sup>,  
A. del Campo<sup>5</sup>, V. Colás<sup>6</sup>, À. Canals<sup>1</sup>, A. Sánchez-Navas<sup>2</sup>, J. Roqué-Rosell<sup>1,4</sup>



doi: 10.7185/geochemlet.2029

## Abstract



Diamond is commonly regarded as an indicator of ultra-high pressure conditions in Earth System Science. This canonical view is challenged by recent data and interpretations that suggest metastable growth of diamond in low pressure environments. One such environment is serpentinisation of oceanic lithosphere, which produces highly reduced  $\text{CH}_4$ -bearing fluids after olivine alteration by reaction with infiltrating fluids. Here we report the first ever observed *in situ* diamond within olivine-hosted,  $\text{CH}_4$ -rich fluid inclusions from low pressure oceanic gabbro and chromitite samples from the Moa-Baracoa ophiolitic massif, eastern Cuba. Diamond is encapsulated in voids below the polished mineral surface forming a typical serpentinisation array, with methane, serpentine and magnetite, providing definitive evidence for its metastable growth upon low temperature and low pressure alteration of oceanic lithosphere and super-reduction of infiltrated fluids. Thermodynamic modelling of the observed solid and fluid assemblage at a reference P-T point appropriate for serpentinisation (350 °C and 100 MPa) is consistent with extreme reduction of the fluid to  $\log f\text{O}_2$  (MPa) = -45.3 ( $\Delta \log f\text{O}_2$  [Iron-Magnetite] = -6.5). These findings imply that the formation of metastable diamond at low pressure in serpentinised olivine is a widespread process in modern and ancient oceanic lithosphere, questioning a generalised ultra-high pressure origin for ophiolitic diamond.

Received 6 June 2020 | Accepted 31 July 2020 | Published 10 September 2020

## Introduction

The discovery of nano- to micrometre scale grains of diamond separated from ophiolitic rocks has recently attracted the attention of geoscientists due to its potential evidence for lithosphere recycling down to, or below, the mantle Transition Zone (e.g., Yang *et al.*, 2007, 2015; Griffin *et al.*, 2016). The earlier reports of diamond in nominally low pressure ophiolitic rocks date back to the early 1990s, when diamond was found in heavy mineral concentrates obtained from Tibetan ophiolites (Bai *et al.*, 1993). These were initially considered to be due to contamination during sample preparation. The debate, however, rejuvenated after findings of other UHP minerals such as coesite together with super-reduced phases in many chromitites and associated peridotites of ophiolites worldwide (e.g., Griffin *et al.*, 2016). Far-reaching geodynamic models have been proposed based on the assumption that diamond growth took place at UHP conditions in these rocks (e.g., Barron *et al.*, 1996; Xiong *et al.*, 2019 and references therein). Recently, the finding of *in situ* diamond in chromite-hosted fluid inclusions from ophiolitic chromitites by Farré-de-Pablo *et al.*, (2019a) provided the first evidence

for empirical (Simakov *et al.*, 2015, 2020), experimental (Simakov *et al.*, 2008) and theoretical (Manuella, 2013; Simakov, 2018) work on low pressure growth of diamond. However, the debate on the natural origin of diamond continued (e.g., Farré-de-Pablo *et al.*, 2019b; Massonne, 2019; Yang *et al.*, 2019). In this regard, Litasov *et al.* (2019a,b) have recently claimed that most diamonds, if not all, from ophiolitic rocks are not natural but instead have a synthetic origin, and emphasised the need to identify diamond below the polished surface of the host mineral. In this study we report for the first time *in situ* diamond grains hosted below the polished surface of magmatic olivine from a low pressure gabbro sill of the upper mantle section of the Moa-Baracoa Ophiolitic Massif, eastern Cuba (Supplementary Information; Figs. S-1-S-4, Table S-1), where super-reduced phases formed during serpentinisation have been previously reported (Pujol-Solà *et al.*, 2018). Diamond grains, which are also present in olivine of associated chromitite, occur in secondary inclusions within olivine. Our observations provide conclusive evidence for the natural formation of metastable diamond at low P (<200 MPa) and low T (<350 °C) during serpentinisation of oceanic mafic and ultramafic rocks, and allow a word of caution

1. Department of Mineralogy, Petrology and Applied Geology, University of Barcelona, Martí i Franquès s/n, 08028 Barcelona, Spain
2. Department of Mineralogy and Petrology, University of Granada, Av. Fuentenueva s/n, 18071 Granada, Spain
3. Andalusian Earth Science Institute (IACT), Spanish Research Council (CSIC)–University of Granada, Av. de las Palmeras 4, 18100 Armilla, Spain
4. Institut de Nanociència i Nanotecnologia, IN2UB Facultat de Química, University of Barcelona, Diagonal 645, 08028 Barcelona, Spain
5. Instituto de Cerámica y Vidrio – CSIC. C. Kelsen, 5, Campus de Cantoblanco, 28049 Madrid, Spain
6. Institute of Geology, National Autonomous University of Mexico, Ciudad Universitaria, 04510 Ciudad de México, Mexico

\* Corresponding author (email: npujolsola@ub.edu)



on the development of generalised geodynamic models of mantle convection and lithosphere recycling into the deep mantle based on diamond and super-reduced phases alone.

## Results

We have studied approximately 150 inclusions (96 below the polished surface) in olivine from 5 gabbro thin sections and 16 inclusions (8 below the surface) hosted in olivine in chromitite (representative inclusions in Table S-2). The inclusions align along trails that extend across adjacent mineral grains and delineate healed fractures (Fig. 1a–d). The distribution of these trails is heterogeneous, with some olivine grains showing a high density of trails cross-cutting each other. Inclusions are typically spheroidal, with sizes ranging between <1 µm and 14 µm in diameter (Figs. 1a–d, S-2).

Diamond grains were identified with the characteristic Raman peak at 1330 cm<sup>-1</sup> with a slight downshift from the typical band to 1326 cm<sup>-1</sup> (n = 17; Table S-2) lining the walls of inclusions (Fig. 1e–f). These very small (200–300 nm) diamond grains were better characterised by confocal Raman maps at different depths (Fig. 1e–h). Nanodiamond is usually associated with methane, serpentine (lizardite, polygonal serpentine, chrysotile), and magnetite (Fig. 1h). Daughter minerals include diopside, chlorite, graphite-like amorphous C, and calcite (Table S-2, Fig. S-5). Brucite was not identified in any of the studied inclusions, similar to other locations (e.g., Sachan *et al.*, 2007). However, brucite is a widespread product in olivine-hosted fluid inclusions in ophiolitic samples (e.g., Klein *et al.*, 2019; Grozeva *et al.*, 2020).

TEM observations of a thin foil extracted by focused ion beam (FIB) (Fig. 2a) reveal that nanodiamond is clearly surrounded by polygonal serpentine and associated with magnetite (Fig. 2b,c). The selected area electron diffraction (SAED) pattern of a grain a few hundreds of nanometres in size confirms its diamond structure (with a reciprocal distance of 5 nm<sup>-1</sup> corresponding to the d<sub>111</sub>-spacing of 2 Å; Fig. 2d), while the corresponding electron energy loss spectrum (EELS) indicates that C-type is the diamond allotrope (sp<sup>3</sup>-hybridised C atoms; Fig. 2e). No polishing debris was observed in the studied inclusions, suggesting no contamination during ion milling of the thin foil except for sublimated Pt used to protect the area. The observed pore space in the inclusions (Figs. 2a, S-6) was likely filled by methane, as indicated by Raman spectroscopy measurements (Table S-2).

Sub-surface fluid inclusions lack water and are dominated by methane (Table S-2), similarly to olivine-hosted fluid inclusions described by Klein *et al.* (2019). In chromitite, diamond grains have been found in 5 sealed fracture-filling inclusions within interstitial magmatic olivine. One inclusion studied by TEM (Fig. S-7) revealed a <1 µm-sized diamond crystal co-existing with the super-reduced phase native Si. In addition, H<sub>2</sub> was identified by Raman spectroscopy in another inclusion (Table S-2). Nevertheless, the phase assemblages are similar to those of the studied inclusions in olivine from the associated gabbro, with serpentine and magnetite (Fig. S-4, Table S-2).

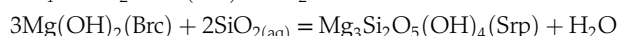
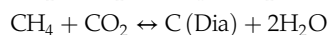
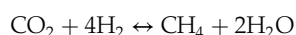
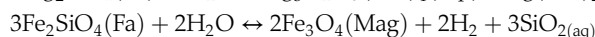
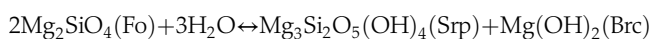
## Natural Origin of the Studied Diamond

The natural *vs.* anthropogenic origin of ophiolitic diamond is a hotly debated topic. Whereas in other samples the natural origin of diamond has not been firmly proved (Massonne, 2019), here we provide several lines of evidence for a natural origin. Our most significant evidence is that diamond is hosted within olivine well below the mineral's polished surface (Fig. 1). Such an observation meets the basic requirements for *in situ* mineral

grains, as suggested by Massonne (2019). Additional evidence includes: (1) that diamond was found within CH<sub>4</sub>-bearing fluid inclusions forming linear arrays (healed fractures) in olivine and surrounded by serpentine (Figs. 1–2), and (2) lack of polishing debris and/or resin artificially incorporated (e.g., Dobrzhinetska *et al.*, 2014).

## Processes and Conditions for Diamond Formation

The olivine-hosted inclusion trails represent fluids trapped in healed fractures. Fluid infiltration in oceanic lithosphere is commonly associated with sporadic deformation events that trigger an increase of porosity by (micro-)fracturing during cooling below the brittle-ductile transition of olivine (Klein *et al.*, 2019). In this scenario, fluid-rock interaction changes from a general open system during initial infiltration to closed system micro-reactors once the inclusions are sealed. At the initial trapping pressure and temperature and during subsequent cooling, the trapped aqueous fluids react with the olivine walls of the inclusion, triggering a number of reactions that ultimately result in growth of hydrated minerals and changes in fluid composition. Comprehensive thermodynamic models of these processes in ultramafic and oceanic rocks (McCollom and Bach, 2009; Klein *et al.*, 2019) show that below ~350 °C (at <200 MPa) in the stability field of serpentine + brucite “serpentinisation” of the walls of olivine hosting fluid inclusions consumes H<sub>2</sub>O in the fluid and generates H<sub>2</sub> through precipitation of Fe<sup>3+</sup>-rich phases, particularly magnetite, so that consumption of inorganic carbon (CO<sub>2</sub>) and formation of abiotic CH<sub>4</sub> takes place. In the 6 component system MgO-FeO-SiO<sub>2</sub>-C-O<sub>2</sub>-H<sub>2</sub>, the formation of phase assemblages made of serpentine, brucite, magnetite, diamond and CH<sub>4</sub>-fluid from an initial assemblage made of olivine and H<sub>2</sub>O-CO<sub>2</sub> fluid can be described by a number of linearly independent reactions. Assuming 11 phase components (Fo, Fa, Mag, Mg-Srp, Mg-Brc, H<sub>2</sub>O, CO<sub>2</sub>, CH<sub>4</sub>, H<sub>2</sub>, SiO<sub>2(aq)</sub>, C abbreviations after Whitney and Evans, 2010) appropriate for the low temperature stage of reaction progress, and excluding magnesite for simplicity, the dimension of the reaction space is 5. Among many, the following set of five linearly independent reactions obtained with the software CSpace (Torres-Roldán *et al.*, 2000) describes the process (commonly used as coupled reactions during serpentinisation, e.g., Lamadrid *et al.*, 2017; Klein *et al.*, 2019):



As a whole, this set of reactions (and any other independent set, provided that it contains all phase components considered) indicates that the hydration process of olivine triggers the formation of magnetite by oxidation of Fe<sup>2+</sup> (from component fayalite), liberating H<sub>2</sub> that ultimately favours the consumption of CO<sub>2</sub> and the formation of CH<sub>4</sub> and C. A bulk mass balance can be obtained after combination of these reactions correspondingly multiplied by a given stoichiometric coefficient. The number of combinations is hence infinite, and combinations that yield zero brucite are possible. A defined mass balance can be calculated only if additional constraints are imposed, such as the bulk composition of the system as long as the relative contribution of the above reactions to the integrated mass balance is a function of the original compositions of olivine and fluid and the initial fluid-olivine ratio. For initial H<sub>2</sub>O-rich fluid and olivine

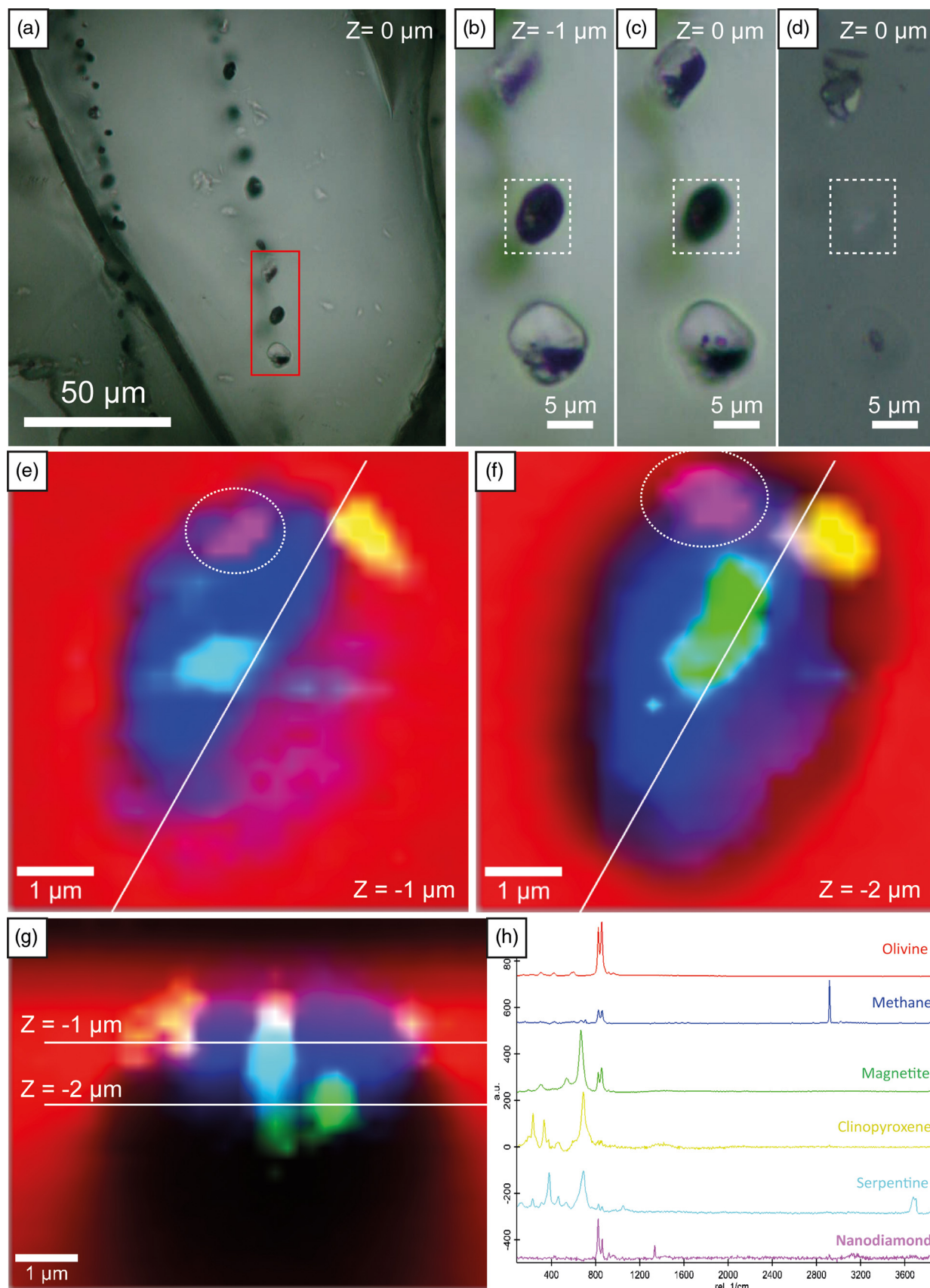


**Figure 1** (a) Transmitted light photomicrograph (TLP) of olivine hosting a trail of secondary fluid inclusions. The red area defines the zoom in (b-d). (b, c) TLP of fluid inclusions below the surface of olivine with focus at  $Z$  (depth) =  $-1$  and  $0 \mu\text{m}$  respectively. (d) Reflected light photomicrograph of (c), showing that the central inclusion is completely below the surface. White rectangles mark the area of (e-g). (e) Fluid inclusion confocal Raman map at  $Z = -1 \mu\text{m}$ ; different colours represent different phases. (f) Confocal Raman map for the same inclusion at  $Z = -2 \mu\text{m}$ . (g) Z-stack of (e, f) showing the inclusion profile. (h) Raman spectra of the identified phases (colour coded). Mapping conditions:  $6 \times 6 \mu\text{m}$ ,  $30 \times 30$  spectra,  $T_{\text{int}} = 2 \text{ s}$ ,  $2 \text{ mW}$ ,  $100\times$  objective.



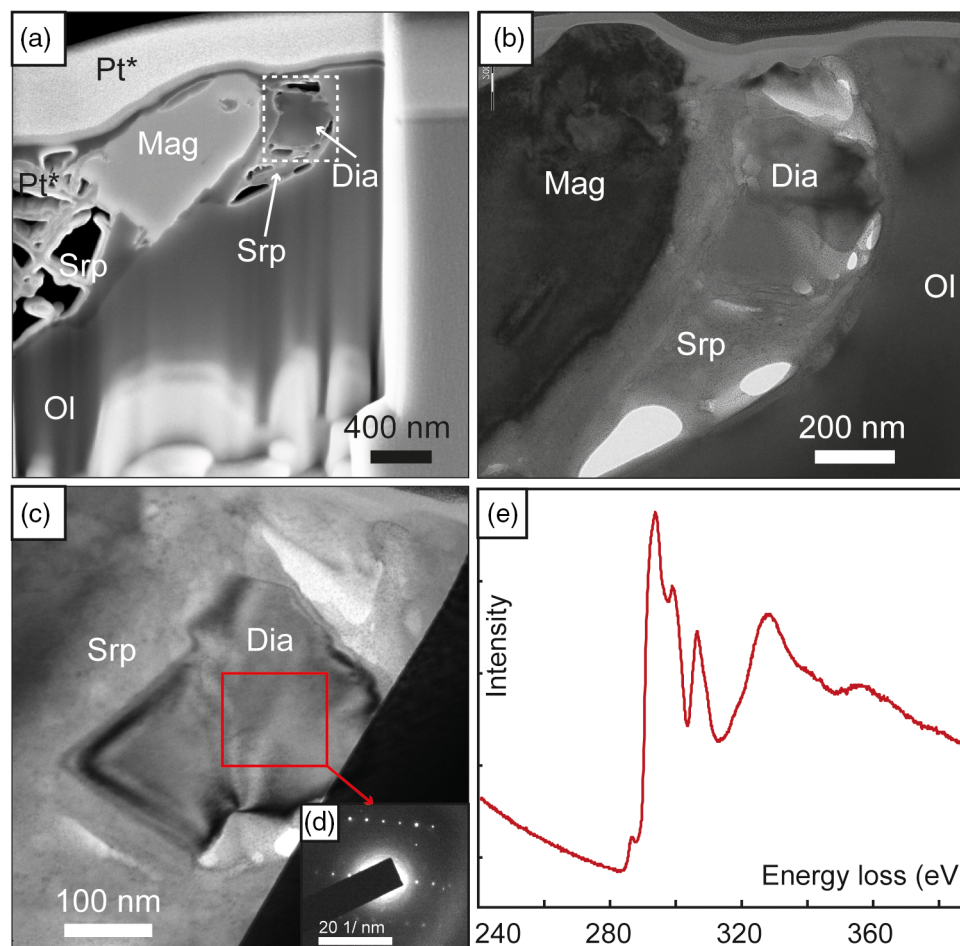
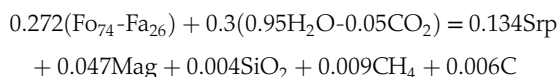


**Figure 2** (a) Field emission scanning electron microscope image of olivine-hosted inclusion thinned by focused ion beam. (b,c) TEM image of the diamond and the surrounding serpentine and magnetite; the red square shows the selected area electron diffraction (SAED). (d) SAED pattern confirming the diamond structure of the crystal (the nearly horizontal rows of reflections have indices 111 with d spacing of 2 Å). (e) Electron energy loss near-edge structure of the C K-edge for the diamond showing a major peak due to its  $sp^3$  bonding. Abbreviations: Dia-Diamond, Mag-magnetite, Ol-olivine, Srp-serpentine, Pt\*-platinum deposited during sample preparation.

with the composition of the studied gabbro (Table S-1), the observed stable brucite-lacking assemblage serpentine + magnetite + diamond +  $CH_4$ -rich fluid can be reached for specific olivine-fluid ratios, such as in the following example obtained using the software CSpace:



This reaction completely consumes both reactants. Under natural conditions in the fluid inclusion, olivine is in excess once  $H_2O$  and  $CO_2$  are completely exhausted. Hence, thermodynamic calculations for a closed system fluid inclusion must consider an olivine-fluid ratio higher than 0.27:0.3. A bulk composition with an initial olivine:fluid ratio of 0.7:0.3 produces an assemblage of 51.3 vol. % Ol (Fo = 0.76), 40.2 vol. % antigorite, 6.8 vol. % magnetite, 1.5 vol. %  $CH_4$  and 0.12 vol. % diamond at 100 MPa and 350 °C using the Perple\_X software (Connolly, 2009). According to the low P conditions at which serpentinisation occurs, the stable C allotrope should be graphite. However, it has been demonstrated that nanodiamond can form at super-reducing conditions (e.g., Manuella, 2013; Simakov, 2018). Hence, in the above thermodynamic calculations, diamond has been used instead of graphite in order to simulate its metastable formation. The corresponding calculated  $\log(fO_2)$  (MPa) is as low as -45.3, ( $\Delta\log fO_2$ [Iron-Magnetite] = -6.5; Frost, 1991),

consistent with thermodynamic calculations in the diamond-COH fluid system at 350 °C and 100 MPa (Fig. 3; cf. Schmidt *et al.*, 2014).

Admittedly, calculations in a more complex system, with additional components and minerals (e.g., CaO, clinopyroxene, talc, carbonates *etc.*) and constraints (e.g., dissolved silica in the fluid), and at other P-T conditions over which serpentinisation takes place, would yield a more intricate picture of the basic process outlined above and different absolute values of  $fO_2$  (e.g., Klein *et al.*, 2019). However, a highly reduced environment (particularly at lower T, see e.g., Klein *et al.*, 2019) should develop if  $CH_4$  is to be the main fluid species in the inclusions, making possible the metastable formation of nanodiamond in low pressure, olivine-bearing oceanic rocks during low T infiltration of  $H_2O$ - $CO_2$  fluid mixtures.

The undoubted natural origin of diamond hosted with serpentine, magnetite and  $CH_4$  in sealed fluid inclusions within magmatic olivine from a gabbro sill and associated chromitite should be related to the generalised release of  $CH_4$  during hydrothermal alteration (partial hydration) of shallow oceanic lithosphere (e.g., Klein *et al.*, 2019). This finding implies that the formation of nanodiamond in altered olivine-bearing rocks can be a widespread process. The presence of diamond (Farré-de-Pablo *et al.*, 2019a) and other highly reduced phases (e.g., metallic Si, moissanite; Pujol-Solà *et al.*, 2018) in these rocks, in

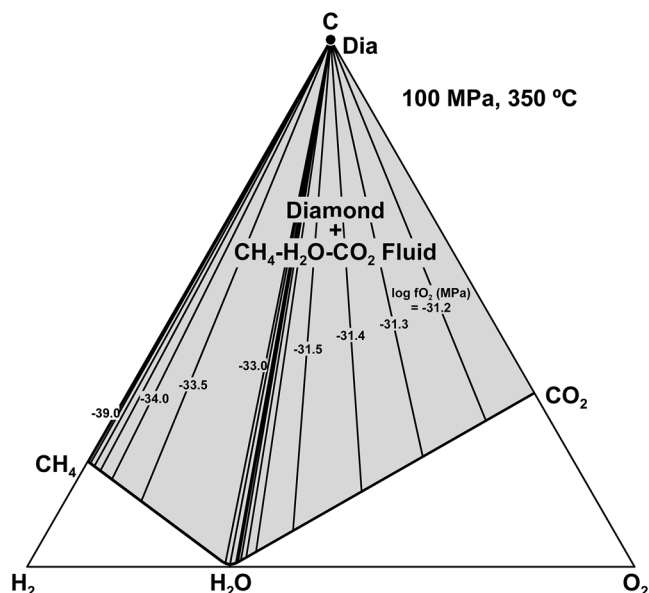


**Figure 3** Phase relations in the C-O-H system (see methods in SI for details) with indication of  $f_{O_2}$  isopleths (black solid lines, log-units) for the diamond-(Dia) saturated portion ( $\log(aC)=0$ ) of the system at 100 MPa, 350 °C.

particular chromitites, cannot hence be taken as a general indication of ultra-high pressure conditions (e.g., Yang *et al.*, 2007, 2015; Griffin *et al.*, 2016). The small size of diamond (<1  $\mu\text{m}$ ) and its scarcity in the fluid inclusions are important handicaps in searching for “the needle in the haystack”, thus explaining its apparent absence in other case studies of altered oceanic rocks.

## Acknowledgements

We thank the editor H.R. Marschall and the reviewers F. Klein, I. Graham and C. Ballhaus for their constructive comments. This research was funded by Fondo Europeo de Desarrollo Regional (FEDER) Funds, Spanish Projects CGL2015-65824, RTI2018-099157-A-I00, PID2019-105625RB-C21, and A.RNM. 186.UGR18. Additional funding was provided by the Ramón y Cajal Fellowship RYC-2015-17596 to JMGJ, a FPU-PhD grant to NPS, the Mexican research programs CONACYT-Ciencia Básica (A1-S-14574) and UNAM-PAPIIT grant IA-101419, and received support for analyses at CIC from the University of Granada.

Editor: Horst R. Marschall

## Additional Information

Supplementary Information accompanies this letter at <http://www.geochemicalperspectivesletters.org/article2029>.



© 2020 The Authors. This work is distributed under the Creative Commons Attribution Non-Commercial No-Derivatives 4.0

License, which permits unrestricted distribution provided the original author and source are credited. The material may not be adapted (remixed, transformed or built upon) or used for commercial purposes without written permission from the author. Additional information is available at <http://www.geochemicalperspectivesletters.org/copyright-and-permissions>.

Cite this letter as: Pujol-Solà, N., Garcia-Casco, A., Proenza, J.A., González-Jiménez, J.M., del Campo, A., Colás, V., Canals, À., Sánchez-Navas, A., Roqué-Rosell, J. (2020) Diamond forms during low pressure serpentinisation of oceanic lithosphere. *Geochem. Persp. Let.* 15, 19–24.

## References

- BAI, W.J., ZHOU, M.F., ROBINSON, P.T. (1993) Possibly diamond-bearing mantle peridotites and podiform chromitites in the Luobusa and Dongqiao ophiolites, Tibet. *Canadian Journal of Earth Sciences* 30, 1650–1659.
- BARRON, L.M., LISHMUND, S.R., OAKES, G.M., BARRON, B.J., SUTHERLAND, F.L. (1996) Subduction model for the origin of some diamonds in the Phanerozoic of eastern New South Wales. *Australian Journal of Earth Sciences* 43, 257–267.
- CONNOLLY, J.A.D. (2009) The geodynamic equation of state: What and how. *Geochemistry, Geophysics, Geosystems* 10, doi: [10.1029/2009GC002540](https://doi.org/10.1029/2009GC002540).
- DOBZHINETSKAYA, L., WIRTH, R., GREEN, H. (2014) Diamonds in Earth's oldest zircons from Jack Hills conglomerate, Australia, are contamination. *Earth and Planetary Science Letters* 387, 212–218.
- FARRÉ-DE-PABLO, J., PROENZA, J.A., GONZÁLEZ-JIMÉNEZ, J.M., GARCÍA-CASCO, A., COLÁS, V., ROQUÉ-ROSELL, J., CAMPRUBÍ, A., SÁNCHEZ-NAVAS, A. (2019a) A shallow origin for diamonds in ophiolitic chromitites. *Geology* 47, 75–78.
- FARRÉ-DE-PABLO, J., PROENZA, J.A., GONZÁLEZ-JIMÉNEZ, J.M., GARCÍA-CASCO, A., COLÁS, V., ROQUÉ-ROSELL, J., CAMPRUBÍ, A., SÁNCHEZ-NAVAS, A. (2019b) A shallow origin for diamonds in ophiolitic chromitites: REPLY. *Geology* 47, e477–e478, doi: [10.1130/G46602Y.1](https://doi.org/10.1130/G46602Y.1).
- FROST, B.R. (1991) Introduction to oxygen fugacity and its petrologic importance. *Reviews in Mineralogy and Geochemistry* 25, 1–9.
- GRIFFIN, W.L., AFONSO, J.C., BELOUSOVA, E.A., GAIN, S.E., GONG, X.H., GONZÁLEZ-JIMÉNEZ, J.M., HOWELL, D., HUANG, J.X., MCGOWAN, N., PEARSON, N.J., SATSUAWA, T., SHI, R., WILLIAMS, P., XIONG, Q., YANG, J.S., ZHANG, M., O'REILLY, S.Y. (2016) Mantle Recycling: Transition Zone Metamorphism of Tibetan Ophiolitic Peridotites and its Tectonic Implications. *Journal of Petrology* 57, 655–684.
- GROZEVA, N.G., KLEIN, F., SEEWALD, J.S., SYLVA, S.P. (2020) Chemical and isotopic analyses of hydrocarbon-bearing fluid inclusions in olivine-rich rocks. *Philosophical Transactions of the Royal Society A: Mathematical, Physical and Engineering Sciences* 378, 20180431.
- KLEIN, F., GROZEVA, N.G., SEEWALD, J.S. (2019) Abiotic methane synthesis and serpentinization in olivine-hosted fluid inclusions. *Proceedings of the National Academy of Sciences of the United States of America* 116, 17666–17672.
- LAMADRID, H.M., RIMSTDT, J.D., SCHWARZENBACH, E.M., KLEIN, F., ULRICH, S., DOLOCAN, A., BODNAR, R.J. (2017) Effect of water activity on rates of serpentinization of olivine. *Nature Communications* 8, 1–9.
- LITASOV, K.D., KAGI, H., VOROPAEV, S.A., HIRATA, T., OHFUJI, H., ISHIBASHI, H., MAKINO, Y., BEKKER, T.B., SEVASTYANOV, V.S., AFANASIEV, V.P., POKHILENKO, N.P. (2019a) Comparison of enigmatic diamonds from the Tolbachik arc volcano (Kamchatka) and Tibetan ophiolites: Assessing the role of contamination by synthetic materials. *Gondwana Research* 75, 16–27.
- LITASOV, K.D., KAGI, H., BEKKER, T.B., HIRATA, T., MAKINO, Y. (2019b) Cuboctahedral type Ib diamonds in ophiolitic chromitites and peridotites: the evidence for anthropogenic contamination. *High Pressure Research* 39, 480–488.
- MANUELLA, F.C. (2013) Can nanodiamonds grow in serpentinite-hosted hydrothermal systems? A theoretical modelling study. *Mineralogical Magazine* 77, 3163–3174.
- MASSONNE, H.J. (2019) Comment: A shallow origin for diamonds in ophiolitic chromitites. *Geology* 47, e476, doi: [10.1130/G46459C.1](https://doi.org/10.1130/G46459C.1).
- MCCOLLOM, T.M., BACH, W. (2009) Thermodynamic constraints on hydrogen generation during serpentinization of ultramafic rocks. *Geochimica et Cosmochimica Acta* 73, 856–875.
- PUJOL-SOLÀ, N., PROENZA, J., GARCÍA-CASCO, A., GONZÁLEZ-JIMÉNEZ, J., ANDREAZINI, A., MELGAREJO, J., GERVILLA, F. (2018) An Alternative Scenario on the Origin of Ultra-High Pressure (UHP) and Super-Reduced (SuR) Minerals in Ophiolitic Chromitites: A Case Study from the Mercedita Deposit (Eastern Cuba). *Minerals* 8, 433, doi: [10.3390/min8100433](https://doi.org/10.3390/min8100433).
- SACHAN, H.K., MUKHERJEE, B.K., BODNAR, R.J. (2007) Preservation of methane generated during serpentinization of upper mantle rocks: Evidence from fluid inclusions in the Nidar ophiolite, Indus Suture Zone, Ladakh (India). *Earth and Planetary Science Letters* 257, 47–59.
- SCHMIDT, M.W., GAO, C., GOLUBKOVA, A., ROHRBACH, A., CONNOLLY, J.A. (2014) Natural moissanite (SiC) – a low temperature mineral formed from highly

- fractionated ultra-reducing COH-fluids. *Progress in Earth and Planetary Science* 1, 27.
- SIMAKOV, S.K. (2018) Nano- and micron-sized diamond genesis in nature: An overview. *Geoscience Frontiers* 9, 1849–1858.
- SIMAKOV, S.K., DUBINCHUK, V.T., NOVIKOV, M.P., DROZDOVA, I.A. (2008) Formation of diamond and diamond-type phases from the carbon-bearing fluid at PT parameters corresponding to processes in the Earth's crust. *Doklady Earth Sciences* 421, 835–837.
- SIMAKOV, S.K., KOUCHI, A., MEL'NIK, N.N., SCRIBANO, V., KIMURA, Y., HAMA, T., SUZUKI, N., SATO, H., YOSHIZAWA, T. (2015) Nanodiamond finding in the hyblean shallow mantle xenoliths. *Scientific Reports* 5, 10765, doi: [10.1038/srep10765](https://doi.org/10.1038/srep10765).
- SIMAKOV, S.K., SCRIBANO, V., MEL'NIK, N.N., BARONE, G. (2020) Sicilian serpentinite xenoliths containing abiotic organics with nanodiamond clusters as key model for prebiotic processes. *Geoscience Frontiers* (in press), doi: [10.1016/j.gsf.2020.04.008](https://doi.org/10.1016/j.gsf.2020.04.008).
- TORRES-ROLDÁN, R.L., GARCIA-CASCO, A., GARCÍA-SÁNCHEZ, P.A. (2000) CSpace: An integrated workplace for the graphical and algebraic analysis of phase assemblages on 32-bit Wintel platforms. *Computers and Geosciences* 26, 779–793.
- WHITNEY, D.L., EVANS, B.W. (2010) Abbreviations for names of rock-forming minerals. *American Mineralogist* 95, 185–187.
- XIONG, F., LIU, Z., KAPSIOTIS, A., YANG, J., LENAZ, D., ROBINSON, P.T. (2019) Petrogenesis of lherzolites from the Purang ophiolite, Yarlung-Zangbo suture zone, Tibet: origin and significance of ultra-high pressure and other 'unusual' minerals in the Neo-Tethyan lithospheric mantle. *International Geology Review* 61, 2184–2210.
- YANG, J.S., DOBRZHINETSAYA, L., BAI, W.J., FANG, Q.S., ROBINSON, P.T., ZHANG, J., GREEN, H.W. (2007) Diamond- and coesite-bearing chromitites from the Luobusa ophiolite, Tibet. *Geology* 35, 875–878.
- YANG, J., MENG, F., XU, X., ROBINSON, P.T., DILEK, Y., MAKEYEV, A.B., WIRTH, R., WIEDENBECK, M., CLIFF, J. (2015) Diamonds, native elements and metal alloys from chromitites of the Ray-Iz ophiolite of the Polar Urals. *Gondwana Research* 27, 459–485.
- YANG, J., LIAN, D., ROBINSON, P.T., QIU, T., XIONG, F., WU, W. (2019) Comment to: A shallow origin for diamonds in ophiolitic chromitites. *Geology* 47, e475, doi: [10.1130/G46446C.1](https://doi.org/10.1130/G46446C.1).

# Diamond forms during low-pressure serpentinitisation of oceanic lithosphere

**N. Pujol-Solà, A. Garcia-Casco, J.A. Proenza, J.M. González-Jiménez, A. del Campo, V. Colás, A. Canals, A. Sánchez-Navas, J. Roqué-Rosell**

## Supplementary Information

The Supplementary Information includes:

- Geological Setting and Petrography
- Methods
- Tables S-1 and S-2
- Figures S-1 to S-7
- Supplementary Information References

### *Geological Setting and Petrography*

The diamond-bearing samples were collected in the Potosí chromitite mining area (20°33'N, 74°45'W) within the Moa-Baracoa Ophiolitic Massif (MBOM; Fig. S-1a), eastern Cuba (Proenza *et al.*, 1999), which forms part of the ca. 1000 km long Cuban ophiolite belt (Late Jurassic - Cretaceous; Iturralde-Vinent *et al.*, 2016 and references therein). The MBOM consists of mantle harzburgites with subordinate dunites and a well-preserved Moho Transition Zone (MTZ), layered gabbros (Fig. S-1b) and mafic volcanic rocks (Marchesi *et al.*, 2006). The mantle tectonites of the MTZ contain elongate dunite bodies, chromitites and gabbroic sill intrusions following the fabric of the host harzburgite, as well as discordant dikes of gabbro, wehrlite and troctolite (Proenza *et al.*, 1999).

In the Potosí area, chromitite bodies are crosscut by several generations of gabbroic intrusions that locally triggered metasomatism in adjacent chromitites (Proenza *et al.*, 2001; González-Jiménez *et al.*, 2020; Pujol-Solà *et al.*, 2020). Diamond grains were found in a gabbro sill formed by a primary assemblage of



olivine (64% vol.; Fo<sub>74</sub>), clinopyroxene (21% vol.; En<sub>37-46</sub>Wo<sub>49-41</sub>Fs<sub>15-9</sub>), plagioclase (14% vol.; An<sub>59-64</sub>), orthopyroxene (1% vol.; En<sub>74-75</sub>) and accessory oxides that show a non-oriented coarse-grained magmatic texture (Figs. S-2, S-3, Table S-1). Diamond was also identified in interstitial magmatic olivine of associated chromitite bodies (Fig. S-4) described in detail by Pujol-Solà *et al.* (2020).

## Methods

### 1. Sample preparation

Olivine gabbro and chromitite samples were collected from the Potosí area in the Moa-Baracoa massif, eastern Cuba. Thin sections were prepared at the University of Barcelona (UB) and the University of Granada (UGR). Thin sections were polished using diamond abrasive paste of 1 µm and 1/4 µm particle size and epoxy resin. Different sets of duplicated thin sections were prepared using Al<sub>2</sub>O<sub>3</sub> or amorphous colloidal silica as carbon-free polishing materials in order to exclude contamination. In addition, ultrasonic baths were performed to remove any remaining polishing debris from the thin sections. Special doubly polished sections approximately 100 µm thick were also prepared for fluid inclusion studies using the same diamond abrasives and using polyester resin.

### 2. Scanning electron microscopy

Samples were studied in detail by optical microscopy and scanning electron microscopy, using a Quanta 200 FEI XTE 325/D8395 scanning electron microscope (SEM) and a JEOL JSM-7100 field-emission scanning SEM at the University of Barcelona (CCiTUB), and also using a GEMINI field-emission scanning SEM at the University of Granada. Operating conditions were 15 – 20 kV accelerating voltage and 5 nA beam current.

### 3. Electron probe microanalyses (EPMA)

Quantitative electron microprobe analyses (EMPA) were conducted at the CCiTUB using a JEOL JXA-8230 electron microprobe and in the Centre for Scientific Instrumentation of the University of Granada (CIC-UGR) using a CAMECA SX100 operated in wavelength-dispersive spectroscopy (WDS) mode. Analytical conditions were 20 kV accelerating voltage, 10-20 nA beam current, 1-2 µm beam diameter, and 10 s counting time per element. Natural and synthetic standards used were Cr<sub>2</sub>O<sub>3</sub> (Cr), wollastonite (Si and Ca), corundum (Al), rutile (Ti), albite (Na), periclase (Mg), hematite (Fe), rhodonite (Mn), orthoclase (K), NiO (Ni), sphalerite (Zn), CaF (F), and NaCl (Cl) at the CCiTUB; and albite (Na), diopside (Si), wollastonite (Ca), vanadinite (Cl), sanidine (K), TiO<sub>2</sub> (Ti), rhodonite (Mn), CaF<sub>2</sub> (F), Fe<sub>2</sub>O<sub>3</sub> (Fe), and synthetic periclase (Mg), Al<sub>2</sub>O<sub>3</sub> (Al), Cr<sub>2</sub>O<sub>3</sub> (Cr), and NiO (Ni) at the CIC-UGR. The correction procedure PAP (Pouchou and Pichoir, 1991) was used to convert specimen intensity ratios into concentrations. The chemical data for Cr-spinel were stoichiometrically recalculated in order to distinguish FeO from Fe<sub>2</sub>O<sub>3</sub> according to the procedure described by Carmichael (1966).

X-ray maps of selected areas were collected with the CAMECA SX100 machine on thin sections using the following analytical conditions: 20 kV accelerating voltage, 300 nA beam current, focused spot, stage-scanning mode, 2 - 8 µm pixel size, and 20 - 30 ms counting time per pixel. The following elements were





mapped: Si, Al, Ba, Ti, Cr, Na, Mg, Mn, Fe, Ni, Ca, K, Cl, Zr, Zn, P, S, and O. The images were treated with DWImager software (Torres-Roldán and Garcia Casco, unpublished; see Garcia-Casco, 2007) and consist of the X-Ray signals of the elements (colour-coded; expressed in counts) and with polish defects, voids and all other mineral masked out. A grey-scale base-layer, calculated with the expression  $\sum(\text{counts}_i \cdot A_i)$  (where  $A$  is atomic number, and  $i$  is Si, Ti, Al, Cr, Fe, Mn, Mg, Ca, Na and K), underlies the images and contains the basic textural information of the scanned areas. Phase abundance maps were created after the manipulation of the histograms of elemental maps.

#### 4. Micro-Raman spectroscopy

Micro-Raman spectra of the solid and fluid inclusions in olivine were obtained using different instruments: a) HORIBA JobinYvon LabRam HR 800 dispersive spectrometer equipped with an Olympus BXFM optical microscope at CCiTUB. Non polarized Raman spectra were obtained in confocal geometry by applying a 532 nm laser, using a 100x objective (beam size around 2  $\mu\text{m}$ ), with 3 - 5 measurement repetitions for 10 - 15 seconds each. The Si band at  $\sim 520\text{ cm}^{-1}$  was used for calibration. The obtained spectra were processed using the LabSpec® software (JobinYvon; Villeneuve-d'Ascq, France); b) JASCO NRS-5100 dispersive spectrometer equipped with an Olympus Optical microscope at CIC-UGR. The spectra conditions were the same as above. The obtained spectra were processed using the Spectra Manager™ II Software and KnowItAll® JASCO Software. The micro-Raman maps were made in two-dimensional mode in the thin sections with 1  $\mu\text{m}$  step and focus at different depth.

Mapping and cross-sections of selected inclusions were taken with a confocal Raman microscope (CRM) at the Instituto de Cerámica y Vidrio (CSIC – Madrid) with spectral resolution of  $0.02\text{ cm}^{-1}$ , coupled with an AFM instrument (Witec ALPHA 300RA), with laser excitation at 532 nm and a 100 $\times$  objective lens ( $\text{NA} = 0.95$ ). The incident laser power was 2 - 6 mW. The optical diffraction resolution was limited to about 200 nm laterally and 500 nm vertically. The samples were mounted in a piezo-driven scan platform having 4 nm lateral and 0.5 nm vertical positioning accuracy, also equipped with an active vibration isolation system, active 0.7 - 1000 Hz. The images were processed and analysed with the software WiTec Project Plus 2.08.

Some inclusions below the polished mineral's surface do not show Raman signal of  $\text{CH}_4$  (or of any other gas species) probably related to the low density of the gas within the inclusion and the detection limit of the Raman analyses (see Grozeva *et al.*, 2020).

#### 5. Focused ion beam (FIB)

A selected inclusion containing diamond hosted in the olivine gabbro was prepared as an electro-transparent thin-foil at the Barcelona Research Center in Multiscale Science and Engineering, from the Polytechnical University of Catalonia (UPC), using a double-beam workstation (Neon40, CarlZeiss) equipped with a Schotky FE-SEM and FIB  $\text{Ga}^+$  columns. The selected inclusion was coated with a thin slip ( $\sim 100\text{ nm}$ ) of Pt by means of e-beam assisted gas deposition as a protection layer for milling and polishing of the thin-foil. Then, the sample was milled by means of Ga ion bombardment until 1  $\mu\text{m}$  thickness. The thin-foil was then lift-out and transferred to a TEM grid using a Kleindiek® micromanipulator with a tungsten tip and fixed into the TEM grid by ion-beam assisted Pt deposition. Finally, the inclusion area within the thin-foil was polished until electron transparency was achieved (down to  $\sim 80\text{ }\mu\text{m}$ ).

A second diamond inclusion within olivine from chromitite was prepared as a thin-foil at the Laboratorio de Microscopías Avanzadas (LMA) from the Universidad de Zaragoza, using a dual beam

Helios Nanolab 650 equipped with a FE-SEM and FIB Ga<sup>+</sup> column. For the thin-foil preparation, the thin section was firstly coated with a thin (a few  $\mu\text{m}$ ) layer of Pd and the area of the inclusion was also coated with a Pt layer by means of e-beam assisted gas deposition for protection of the interest area. The preparation of the thin-foil followed the same process as described above, but it was transferred to the grid using an Omniprobe® nanomanipulator.

## 6. Transmission electron microscopy (TEM)

The TEM study on the first thin-foil (olivine gabbro) was performed at the CCiTUB with a JEOL JEM-2100 LaB<sub>6</sub> transmission electron microscope (TEM) with energy dispersed analysis of X-rays (EDX), operated at 200 kV in STEM mode and beam size of  $\sim 15$  nm, with an Oxford Instruments INCA x-sight spectrometer with Si (Li) detector. Images were acquired using a Gatan CCD Camera Orius SC1000 and processed with the DigitalMicrograph™ Software (v. 1.71.38).

The second thin-foil (chromitite) was studied using a FEI Titan G2 TEM equipped with Field Emission cannon XFEG, with spherical correction for the objective lens and working at 300 kV at the CIC-UGR. The microscope is equipped with four energy-dispersive analyses of X-rays (EDX) detectors (FEI microanalysis Super X) that allowed to perform elemental maps, and high angle-annular dark field detector (HAADF) that allowed to obtain high Z contrast mages. High-magnification electron microscopy (HMEM) images and selected area electron diffraction (SAED) patterns were also acquired. Images were processed with Digital Micrograph® Software (v. 1.71.38) and maps with INCA® Microanalysis Suite Software (v. 4.09).

## 7. Electron energy loss spectroscopy (EELS)

The electron energy loss spectroscopy (EELS) was performed at the CIC-UGR using a Zeiss Libra 120 plus LaB<sub>6</sub> transmission electron microscope with Omega energy filtering, operating at 120 kV. Analyses were done at 80000x magnification with 1 - 2  $\mu\text{A}$  current emission on an area of 300 nm of diameter.

## 8. Thermodynamic calculations

The thermodynamic calculations were performed using Perple\_X 6.8.3 (Connolly, 2009; <http://www.perplex.ethz.ch/>) and the internally consistent thermodynamic database of Holland and Powell (2011) extended to include super-reduced phases (cr\_hp11ver\_metal.dat). In the above database we removed graphite in order to simulate the metastable formation of diamond. The solution models considered were olivine (Holland and Powell, 1998) and C-O-H fluid (Connolly and Cesare, 1993). All other minerals involved in the calculations were treated as pure phases. Phase relations for olivine-hosted CH<sub>4</sub>-rich fluid inclusions were computed at 100 MPa and 350 °C in the system MgO-FeO-SiO<sub>2</sub>-C-O<sub>2</sub>-H<sub>2</sub> (MFSCOH). The bulk composition of the fluid inclusion-olivine ensemble corresponds to an initial assemblage of 0.7:0.3 molar mix of magmatic olivine (Fo<sub>74</sub>, (Mg<sub>1.48</sub>Fe<sub>0.52</sub>)SiO<sub>4</sub>) and H<sub>2</sub>O-rich fluid ( $X_{\text{H}_2\text{O}} = 0.95$ , 0.95H<sub>2</sub>O:0.05CO<sub>2</sub>). The phase relations for diamond-COH fluid (Fig. 3) were computed in the C-O-H system and contoured for oxygen fugacity isopleths calculated for a diamond-buffered fluid (Connolly and Cesare, 1993).

## Tables S-1 to S-2

**Table S-1** Representative electron microprobe analyses of olivine in the studied samples.

Sample	POT-2(II)					POT-2B					POT-3				
Analyse	ol-1	ol-2	ol-3	ol-4	ol-5	ol-1	ol-2	ol-3	ol-4	ol-5	ol-1	ol-2	ol-3	ol-4	ol-5
SiO <sub>2</sub> (wt.%)	38.26	38.17	38.03	37.70	37.75	37.59	37.55	37.45	37.65	38.02	40.54	40.47	40.68	40.49	40.59
TiO <sub>2</sub>	bdl	bdl	bdl	bdl	bdl	0.02	bdl	bdl	0.02	bdl	bdl	bdl	bdl	bdl	0.02
Al <sub>2</sub> O <sub>3</sub>	bdl	bdl	bdl	bdl	bdl	bdl	0.02	0.03	bdl	bdl	bdl	bdl	0.02	bdl	0.03
Cr <sub>2</sub> O <sub>3</sub>	bdl	bdl	bdl	bdl	bdl	bdl	bdl	bdl	bdl	bdl	bdl	0.06	0.05	0.03	bdl
FeO <sub>t</sub>	24.03	24.19	24.23	24.15	24.22	24.78	24.33	24.70	24.30	24.28	9.90	9.96	9.61	10.03	9.70
MnO	0.35	0.34	0.36	0.37	0.36	0.36	0.39	0.38	0.38	0.38	0.14	0.16	0.16	0.17	0.16
MgO	37.79	37.76	37.45	37.34	37.47	36.80	36.80	36.47	36.86	37.25	48.75	48.55	48.70	48.94	48.74
NiO	0.15	0.14	0.16	0.15	0.16	0.14	0.18	0.15	0.12	0.15	0.27	0.28	0.26	0.28	0.29
CaO	0.05	0.04	0.03	0.02	0.03	0.03	0.03	0.05	0.04	0.02	0.02	0.02	0.02	0.03	0.02
Total	100.63	100.64	100.26	99.73	99.99	99.73	99.31	99.23	99.37	100.10	99.62	99.49	99.50	99.97	99.55
Cations per 4 oxygens															
Si	0.997	0.996	0.996	0.994	0.993	0.994	0.995	0.995	0.997	0.998	0.999	0.998	1.002	0.995	0.999
Ti						0.000			0.000						0.000
Al							0.001	0.001					0.001		0.001
Cr												0.001	0.001	0.001	
Fe <sup>2+</sup>	0.524	0.528	0.531	0.532	0.533	0.548	0.539	0.549	0.538	0.533	0.204	0.206	0.198	0.206	0.200
Mn	0.008	0.008	0.008	0.008	0.008	0.008	0.009	0.008	0.009	0.008	0.003	0.003	0.003	0.004	0.003
Mg	1.468	1.469	1.463	1.467	1.469	1.450	1.454	1.445	1.455	1.458	1.790	1.786	1.787	1.792	1.789
Ni	0.003	0.003	0.003	0.003	0.003	0.003	0.004	0.003	0.003	0.003	0.005	0.005	0.005	0.005	0.006
Ca	0.001	0.001	0.001	0.001	0.001	0.001	0.001	0.001	0.001	0.001	0.000	0.000	0.000	0.001	0.001
Total	3.002	3.004	3.003	3.006	3.007	3.005	3.003	3.003	3.002	3.001	3.001	3.000	2.997	3.003	2.999
Fo	0.74	0.74	0.73	0.73	0.73	0.73	0.73	0.72	0.73	0.73	0.90	0.90	0.90	0.90	0.90
Ni (ppm)	1288	1143	1366	1257	1310	1137	1529	1301	1040	1260	2309	2323	2178	2319	2468



**Table S-2** Selected representative studied inclusions in olivine from the Potosí gabbro (POT-2) and chromitite (POT-3).

Sample	Host rock	Number	In surface/ sealed	Inclusion abundance	Size (µm)	Species													
						Lizardite	Polygonal serpentine	Magnetite	CH <sub>4</sub>	cm <sup>-1</sup>	H <sub>2</sub>	cm <sup>-1</sup>	Amorphous C / graphite	Diamond	cm <sup>-1</sup>	Calcite	Clinopyroxene	Chlorite	Native Si
POT-2(II)	Gabbro	1	Surface	++	4			X						X	1332	X			
POT-2(II)	Gabbro	2	Surface	++	2			X						X	1328	X			
POT-2(II)	Gabbro	3	Surface	++	4			X					X	X	1328				
POT-2(II)	Gabbro	4	Surface	++	6			X						X	1326	X			
POT-2(II)	Gabbro	5	Surface	++	5			X					X	X	1330				
POT-2(II)	Gabbro	6	Surface	+++	1								X			X			
POT-2_AI	Gabbro	7	Sealed	++	4			X	X	2913									
POT-2_AI	Gabbro	8	Sealed	++	4			X											
POT-2_AI	Gabbro	9	Sealed	++	4				X	2915									
POT-2B_Si	Gabbro	10	Sealed	++	4	X		X											
POT-2B_Si	Gabbro	11	Sealed	++	4	X		X											
POT-2B_Si	Gabbro	12	Sealed	++	4	X		X											
POT-2B_Si	Gabbro	13	Sealed	++	2	X		X											
POT-2B_Si	Gabbro	14	Sealed	++	2	X		X											
POT-2B_Si	Gabbro	15	Sealed	++	2	X													
POT-2B_Si	Gabbro	16	Sealed	++	2	X		X											
POT-2B_Si	Gabbro	17	Sealed	++	2	X			X	2915									
POT-2B_Si	Gabbro	18	Sealed	++	2	X			X	2917									
POT-2B_Si	Gabbro	19	Surface	++	2	X													
POT-2B_Si	Gabbro	20	Sealed	++	3	X			X	2915									
POT-2B_Si	Gabbro	21	Sealed	++	3		X	X	X	2915									
POT-2B_Si	Gabbro	22	Sealed	++	2		X		X	2915									
POT-2B_Si	Gabbro	23	Sealed	++	2		X		X	2915									
POT-2B_Si	Gabbro	24	Sealed	++	2	X		X	X	2915									
POT-2B_Si	Gabbro	25	Sealed	++	1								X						
POT-2B_Si	Gabbro	26	Sealed	++	1	X		X	X	2913									
POT-2B_Si	Gabbro	27	Sealed	+	2	X			X	2915									
POT-2B_Si	Gabbro	28	Sealed	+	2		X		X	2915									
PO-2_IF	Gabbro	29	Sealed	+	2			X											
PO-2_IF	Gabbro	30	Sealed	++	5	X		X	X	2912			X	X	1330		X		
PO-2_IF	Gabbro	31	Surface	++	5				X				X	X					
PO-2_IF	Gabbro	32	Sealed	++	2	X			X	2913									
PO-2_IF	Gabbro	33	Sealed	++	2	X			X	2915									
PO-2_IF	Gabbro	34	Surface	++	2	X								X	1331				
PO-2_IF	Gabbro	35	Sealed	++	2									X	1330				
PO-2_IF	Gabbro	36	Sealed	+++	5			X	X	2919									
PO-2_IF	Gabbro	37	Sealed	+++	5			X											



Sample	Host rock	Number	In surface/ sealed	Inclusion abundance	Size (µm)	Species													
						Lizardite	Polygonal serpentine	Magnetite	CH <sub>4</sub>	cm <sup>-1</sup>	H <sub>2</sub>	cm <sup>-1</sup>	Amorphous C / graphite	Diamond	cm <sup>-1</sup>	Calcite	Clinopyroxene	Chlorite	Native Si
PO-2_IF	Gabbro	38	Surface	+	5	X		X											
PO-2_IF	Gabbro	39	Surface	+	5	X													
PO-2_IF	Gabbro	40	Surface	++	2	X							X	X	1329				
PO-2_IF	Gabbro	41	Sealed	++	3	X		X	X	2915									
POT-2c	Gabbro	42	Surface	+	4			X											
POT-2c	Gabbro	43	Surface	+	2	X		X											
POT-2c	Gabbro	44	Sealed	++	5	X		X	X	2916									
POT-2c	Gabbro	45	Sealed	++	4	X		X	X	2916									
POT-2c	Gabbro	46	Sealed	++	4	X		X		2914									
POT-2c	Gabbro	47	Sealed	++	2	X			X	2916									
POT-2c	Gabbro	48	Sealed	++	4			X	X	2916									
POT-2c	Gabbro	49	Sealed	++	4	X		X	X	2916									
POT-2c	Gabbro	50	Sealed	++	5				X	2918									
POT-2c	Gabbro	51	Sealed	++	4				X	2919									
POT-2c	Gabbro	52	Sealed	++	4			X											
POT-2c	Gabbro	53	Sealed	++	4	X		X	X	2918									
POT-2c	Gabbro	54	Sealed	++	5				X	2919									
POT-2c	Gabbro	55	Sealed	++	4				X	2918									
POT-2c	Gabbro	56	Sealed	++	5			X	X	2918									
POT-2c	Gabbro	57	Sealed	++	5	X		X	X	2916									
POT-2c	Gabbro	58	Sealed	++	5	X		X	X	2916									
POT-2c	Gabbro	59	Sealed	+	1			X											
POT-2c	Gabbro	60	Sealed	+	3			X											
POT-2c	Gabbro	61	Sealed	++				X											
POT-2c	Gabbro	62	Sealed	++		X		X											
POT-2c	Gabbro	63	Sealed	++				X											
POT-2c	Gabbro	64	Sealed	++				X											
POT-2c	Gabbro	65	Sealed	++				X											
POT-2c	Gabbro	66	Sealed	++				X											
POT-2c	Gabbro	67	Sealed	++				X											
POT-2c	Gabbro	68	Sealed	++				X											
POT-2c	Gabbro	69	Sealed	++															
POT-2c	Gabbro	70	Sealed	++				X										X	
POT-2c	Gabbro	71	Sealed	++		X		X	X	2917									
POT-2c	Gabbro	72	Sealed	++		X		X	X	2917									
POT-2c	Gabbro	73	Sealed	++		X		X											
POT-2c	Gabbro	74	Sealed	++		X		X											
POT-2c	Gabbro	75	Sealed	++					X	2917									
POT-2c	Gabbro	76	Sealed	++		X		X											
POT-2c	Gabbro	77	Sealed	++		X		X	X	2917									
POT-2c	Gabbro	78	Sealed	++		X		X											
POT-2c	Gabbro	79	Sealed	++		X		X											

Sample	Host rock	Number	In surface/ sealed	Inclusion abundance	Size (µm)	Species													
						Lizardite	Polygonal serpentine	Magnetite	CH <sub>4</sub>	cm <sup>-1</sup>	H <sub>2</sub>	cm <sup>-1</sup>	Amorphous C / graphite	Diamond	cm <sup>-1</sup>	Calcite	Clinopyroxene	Chlorite	Native Si
POT-2c	Gabbro	80	Sealed	++	4	X		X	X	2917									
POT-2c	Gabbro	81	Sealed	++		X		X											
POT-2c	Gabbro	82	Sealed	++		X		X											
POT-2c	Gabbro	83	Sealed	++		X		X											
POT-2c	Gabbro	84	Sealed	++		X		X											
POT-2c	Gabbro	85	Sealed	++		X		X											
POT-2c	Gabbro	86	Sealed	++				X											
POT-2c	Gabbro	87	Sealed	++		X		X											
POT-2c	Gabbro	88	Sealed	++	12	X		X	X	2917							X		
POT-2c	Gabbro	89	Sealed	++		X		X											
POT-2c	Gabbro	90	Sealed	++		X													
POT-2c	Gabbro	91	Sealed	++		X													
POT-2c	Gabbro	92	Sealed	++		X		X											
POT-3	Chromitite	93	Surface	+++										X	1331				X
POT-3	Chromitite	94	Sealed	+++		X		X											
POT-3	Chromitite	95	Sealed	+++										X	1329				
POT-3	Chromitite	96	Sealed	+++		X													
POT-3	Chromitite	97	Sealed	+++										X	1330				
POT-3	Chromitite	98	Sealed	+++										X					
POT-3	Chromitite	99	Sealed	+++							X	4154							
POT-3	Chromitite	100	Surface	+++	1														

## Figures S-1 to S-7

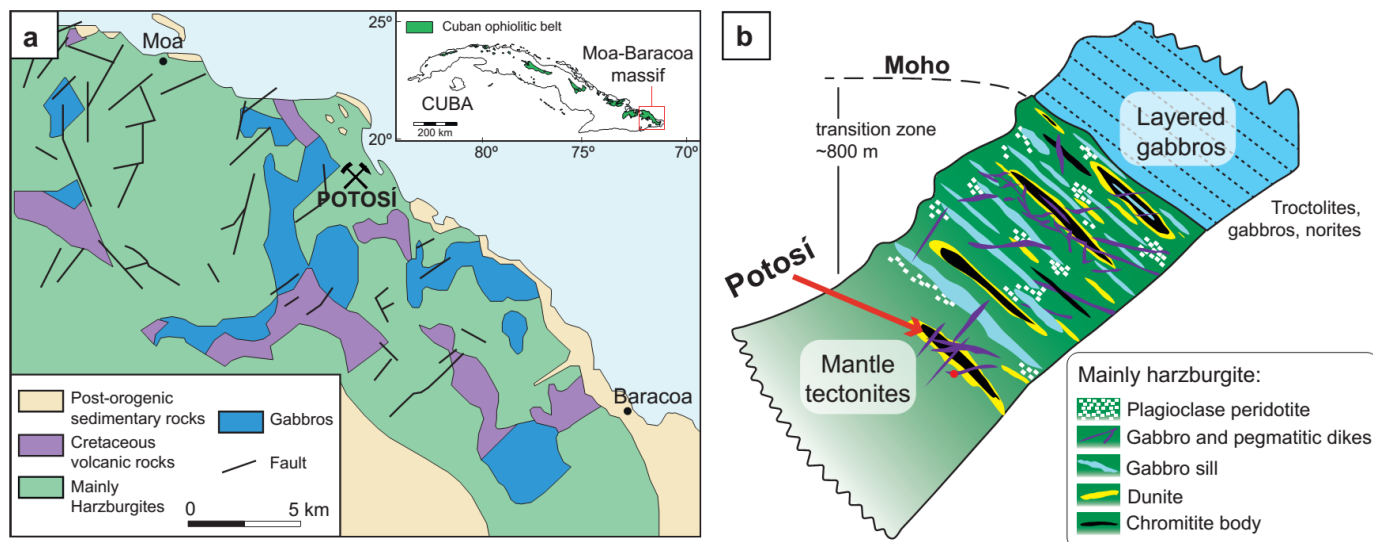


**Figure S-1** (a) Geological map of the Moa-Baracoa massif in eastern Cuba, modified from Proenza *et al.* (2001). The inset in the upper right shows the location within the Cuba Island. (b) Schematic column of the ophiolitic sequence in the Moa Baracoa Massif (eastern Cuba) showing the position of the Potosí chromitites, modified from Marchesi *et al.* (2006).

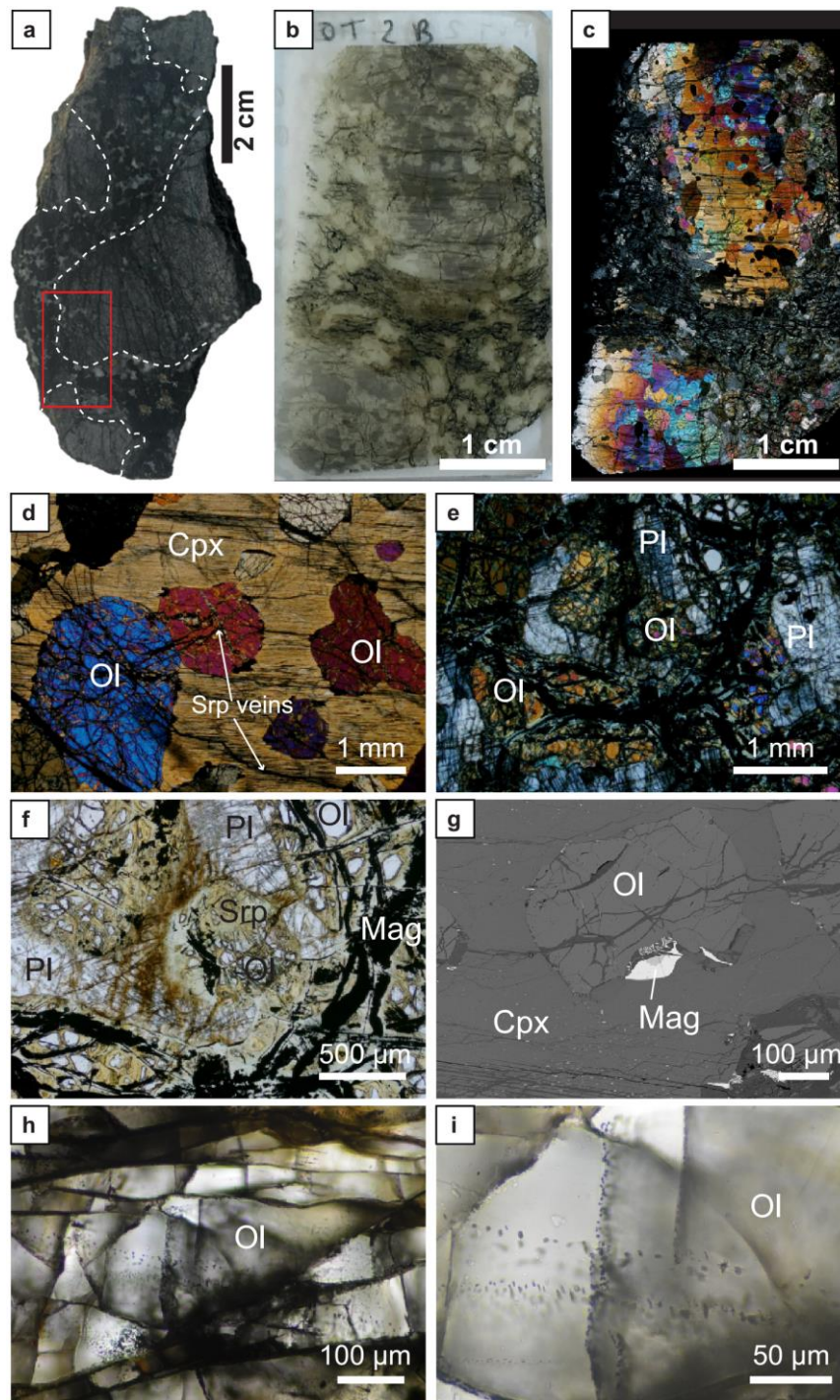


**Figure S-2** (a) Diamond-bearing olivine gabbro hand sample. The red rectangle marks the area of the thin section in b-c. (b) Thin section of the olivine gabbro. (c) Thin section of the olivine gabbro in crossed nicols. Note the poikilitic texture of the sample. (d) Transmitted light (crossed nicols) photomicrograph of the olivine gabbro showing the poikilitic texture of clinopyroxene and olivine. (e) Transmitted light (crossed nicols) photomicrograph of the olivine gabbro showing the poikilitic texture of partially altered plagioclase and olivine. (f) Transmitted light photomicrograph of partially serpentinised olivine with serpentine-group minerals and magnetite veins. (g) Backscattered electron image of an olivine chadacryst with magnetite in a larger poikilitic clinopyroxene crystal. (h) Transmitted light photomicrograph of olivine hosting multiple trails of fluid inclusions with crosscutting relations. (i) Transmitted light photomicrograph of a close up of fluid inclusion trails hosted in olivine. Abbreviations: Cpx – clinopyroxene, Mag – magnetite, Ol – olivine, Pl – plagioclase, Srp – serpentine.



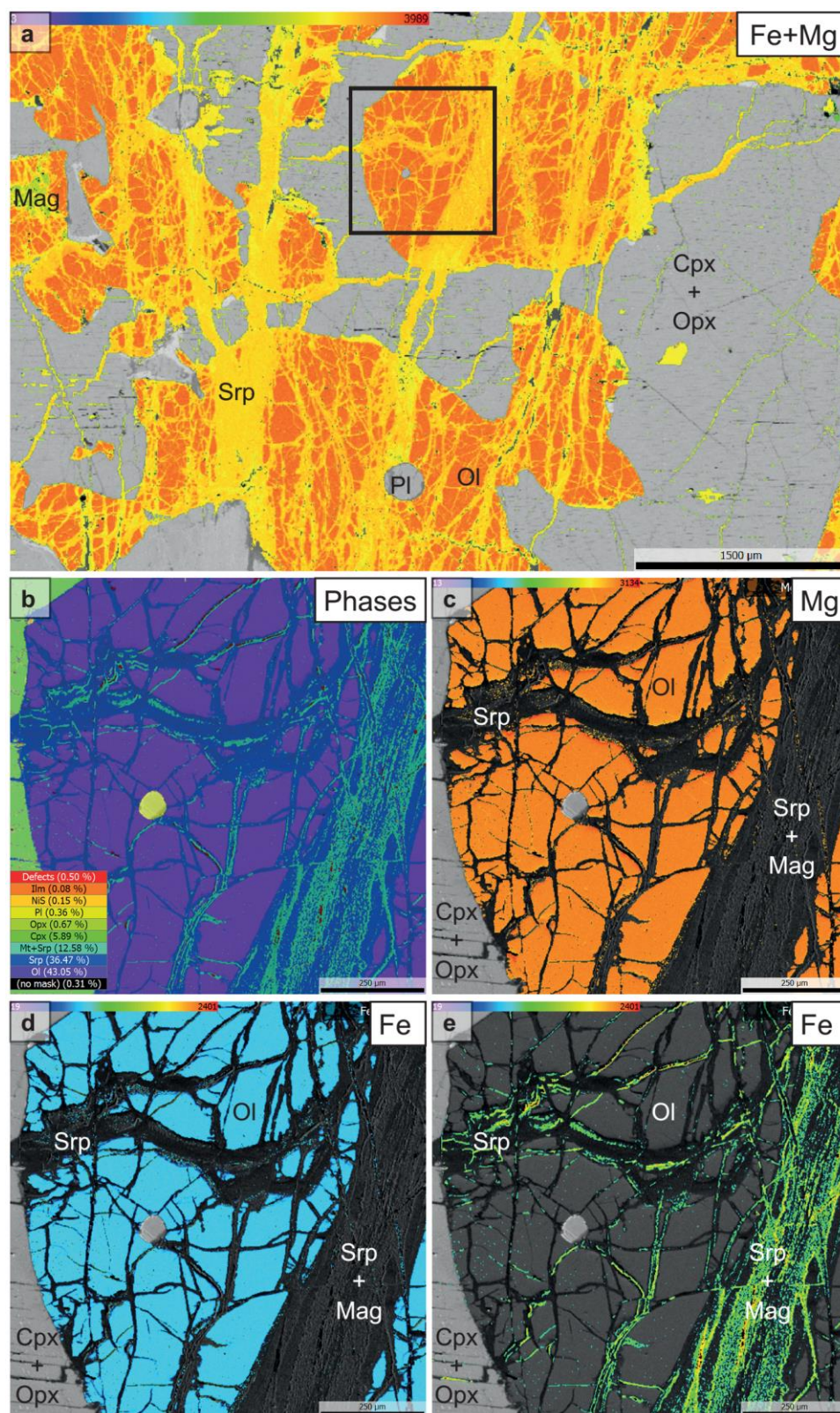


**Figure S-3** Electron microprobe X-ray maps of the olivine gabbro. **(a)** Fe+Mg element map of olivine crystals and serpentine veins cross cutting the sample. The black square marks the area of the detailed maps b-e. **(b)** Phase map of the analysed area. **(c)** Mg map of olivine. **(d)** Fe map of olivine. **(e)** Fe map of the serpentine veins containing magnetite. Abbreviations: Cpx – clinopyroxene, Opx – orthopyroxene, Mag – magnetite, Ol – olivine, Pl – plagioclase, Srp – serpentine.



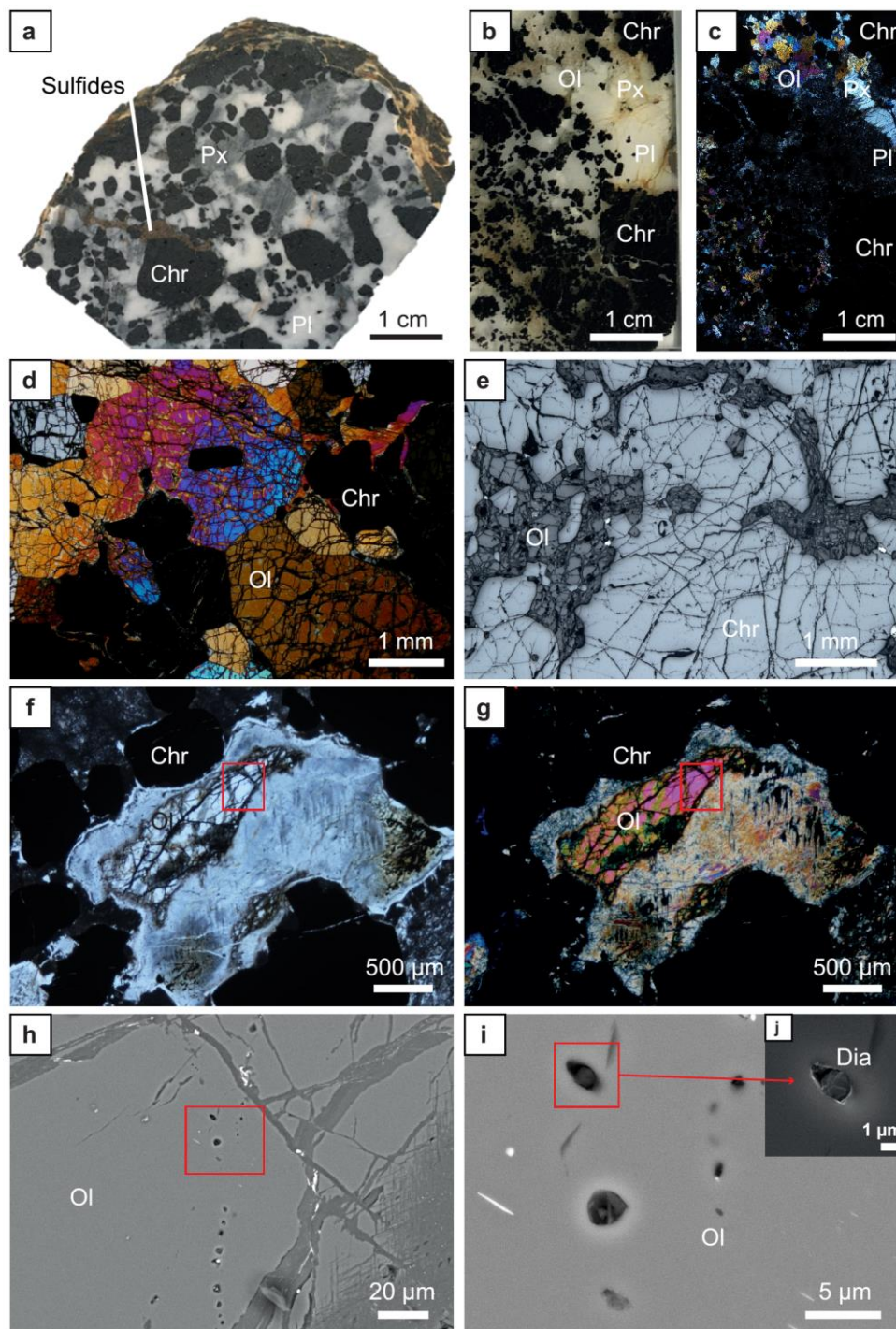


**Figure S-4** (a) Diamond-bearing chromitite hand sample. (b) Thin section of the chromitite. (c) Thin section of the chromitite in crossed nicols. (d) Transmitted light (crossed nicols) microphotograph of chromitite showing interstitial magmatic olivine. (e) Reflected light microphotograph of chromite and interstitial olivine. (f) Transmitted light microphotograph of partially altered olivine hosting inclusion trails. (g) Transmitted light (crossed nicols) microphotograph of partially altered olivine hosting inclusion trails. The red rectangle marks the area of image h. (h) Backscattered electron image of inclusion trails hosted within olivine. The red rectangle marks the area of image i. (i) Backscattered electron image of inclusions hosting diamond and native Si (top) and serpentine (center): needle-like crystal is ilmenite and the bright dot is chromite. (j) Zoom of i showing a secondary electron image of the inclusion hosting diamond and native Si. Abbreviations: Chr – chromite, Dia - diamond, Mag – magnetite, Ol – olivine, Pl – plagioclase, Px – pyroxene.

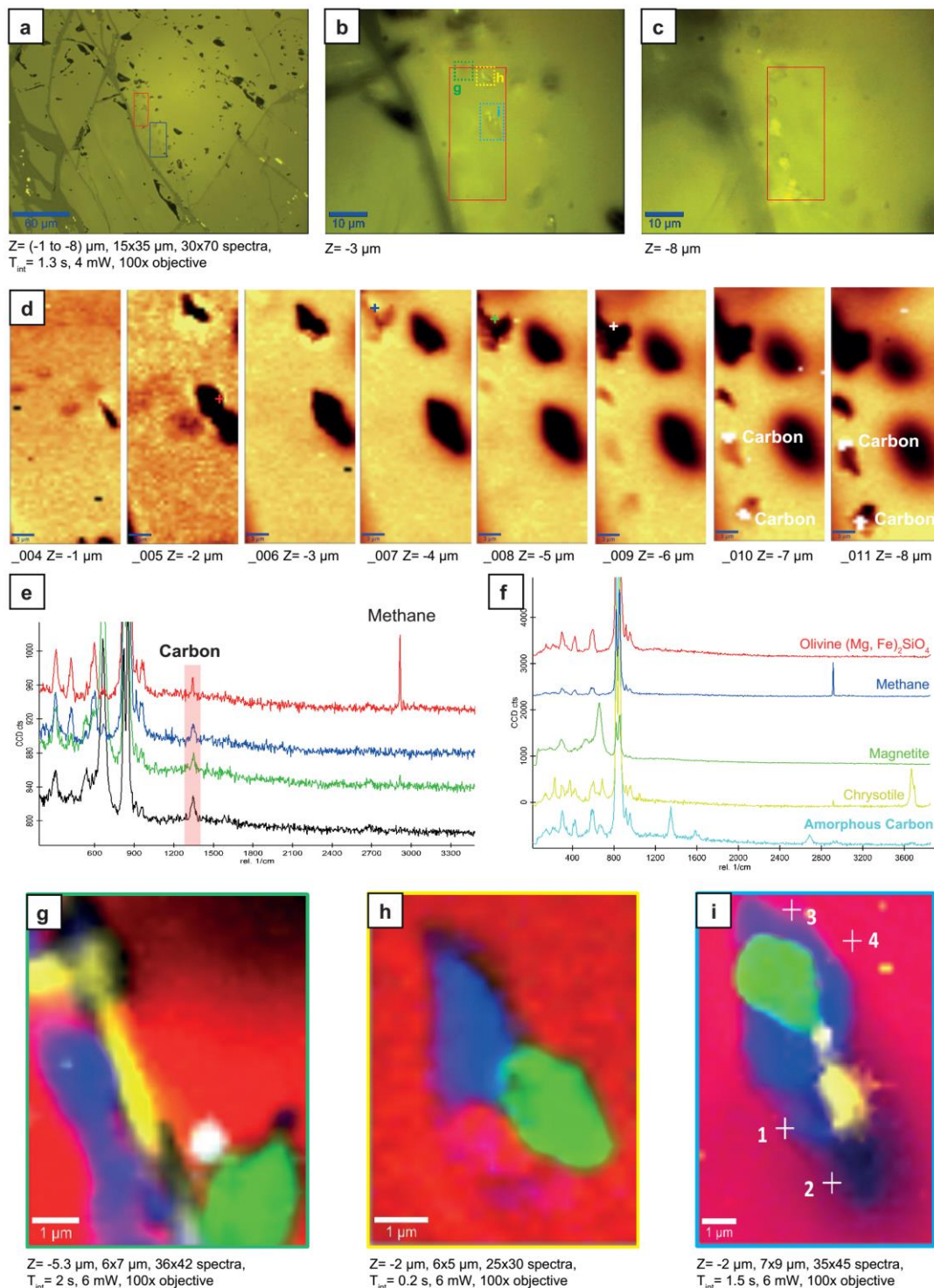


**Figure S-5** Confocal Raman maps of fluid inclusions. **(a)** Reflected light microphotograph of inclusion trails hosted in olivine from the gabbro. **(b)** Zoom of **(a)** showing the inclusions at Z (depth) = -3 μm. **(c)** Image **(b)** with focus at Z = -8 μm. Note that the inclusions that are shown in **(b)** and **(c)** are different. **(d)** Z-stack in the area in red in **(b)** and **(c)** from Z = -1 μm to Z = -8 μm. Amorphous carbon has been recognized in 5 inclusions. **(e)** Amorphous carbon Raman patterns corresponding to the inclusions in the Z-stack of **(d)**. The colors correspond to the analyzed points showed in **(d)**. **(f)** Raman spectra for the different phases observed in the inclusion maps **(g-i)**. **(g)** X-Y Raman map of the inclusion denoted by the green square in **(b)**. **(h)** X-Y Raman map of the inclusion denoted by the yellow square in **(b)**. **(i)** X-Y Raman map of the inclusion denoted by the blue square in **(b)**.



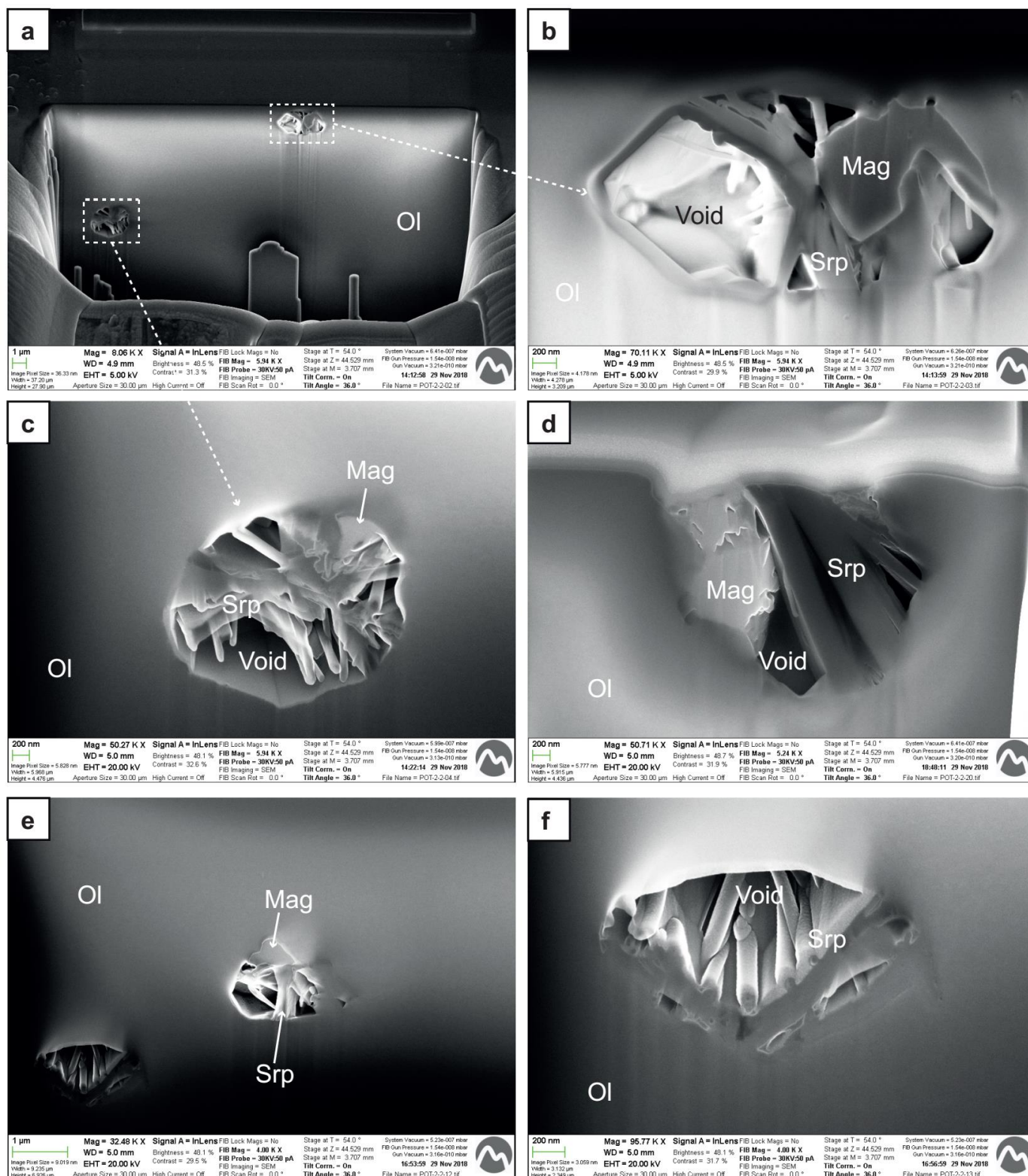


**Figure S-6** Backscattered electron images of inclusions hosted within olivine cut with focused ion beam (FIB). Most inclusions contain serpentine and magnetite. Abbreviations: Mag – magnetite, Ol – olivine, Srp – serpentine.



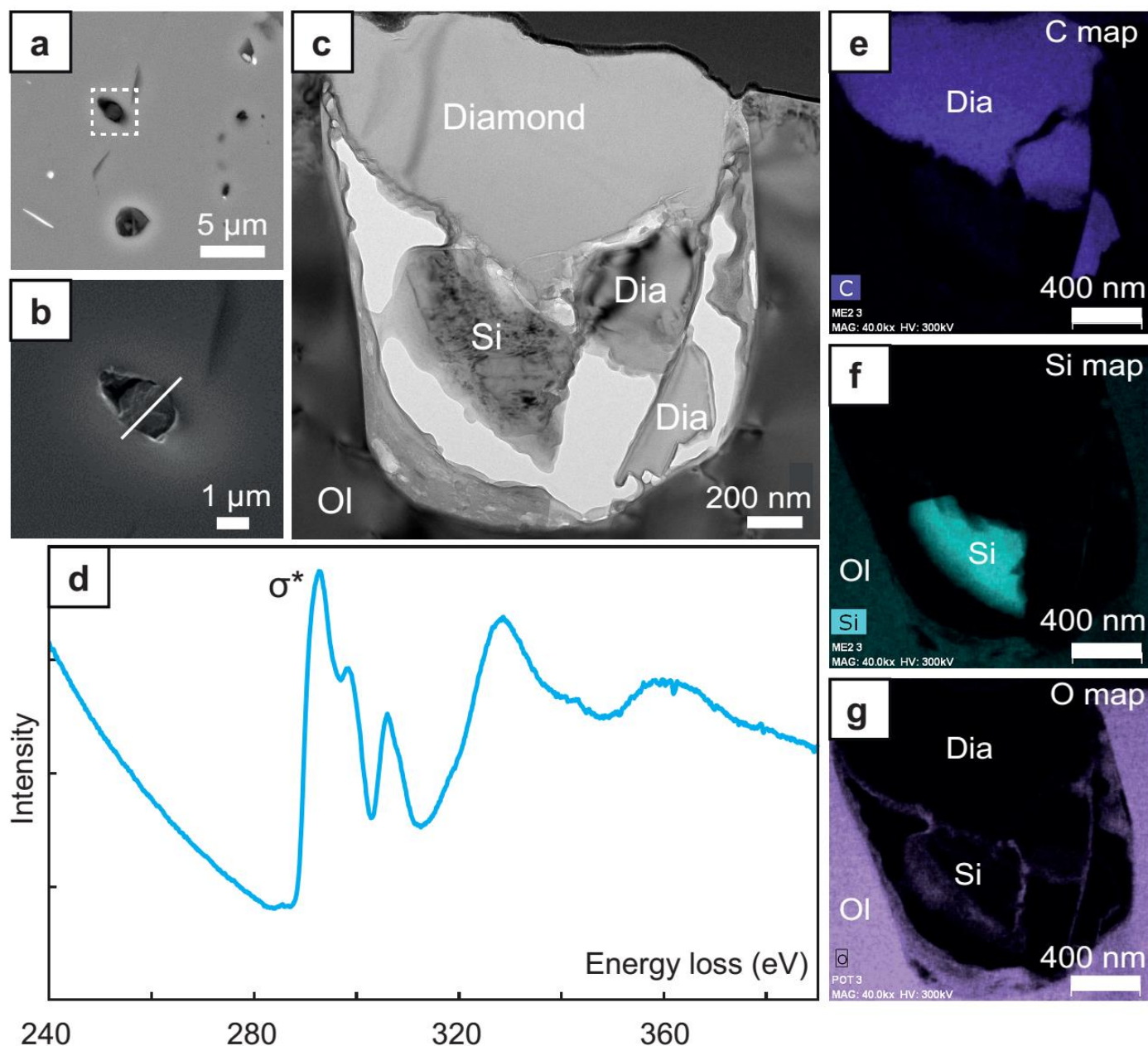


**Figure S-7** Diamond hosted in interstitial olivine in chromitite. (a) Field-emission scanning electron microscope (FE-SEM) back-scattered image showing the location of a diamond grain in olivine. (b) Detailed FE-SEM secondary electron image of the diamond grain cut with focused ion beam (FIB). (c) Transmission electron microscopy (TEM) image showing the grains of diamond and native Si. (d) ELNES of C-K at the diamond grain, indicating the  $sp^3$  hybridization of C by the presence of a strong  $\sigma^*$  peak at about 290 eV, but no  $\Pi^*$  peak. (e-g) TEM X-ray maps of C, Si and O, respectively. Abbreviations: Dia- diamond, Ol – olivine, Si – native silicon.

## Supplementary Information References

- Carmichael, I.S.E. (1966) The iron-titanium oxides of salic volcanic rocks and their associated ferromagnesian silicates. *Contributions to Mineralogy and Petrology* 14, 36–64.
- Connolly, J.A.D. (2009) The geodynamic equation of state: What and how. *Geochemistry, Geophysics, Geosystems* 10.
- Connolly, J.A.D., Cesare, B. (1993) C-O-H-S fluid composition and oxygen fugacity in graphitic metapelites. *Journal of Metamorphic Geology* 11, 379–388.
- García-Casco, A. (2007) Magmatic paragonite in trondhjemites from the Sierra del Convento mélange, Cuba. *American Mineralogist* 92, 1232–1237.
- González-Jiménez, J.M., Proenza, J.A., Pastor-Oliete, M., Saunders, E., Aiglsperger, T., Pujol-Solà, N., Melgarejo, J.C., Gervilla, F., García-Casco, A. (2020) Precious metals in magmatic Fe-Ni-Cu sulfides from the Potosí chromitite deposit, eastern Cuba. *Ore Geology Reviews* 118, 103339.
- Grozeva, N.G., Klein, F., Seewald, J.S., Sylva, S.P. (2020) Chemical and isotopic analyses of hydrocarbon-bearing fluid inclusions in olivine-rich rocks. *Philosophical transactions. Series A, Mathematical, physical, and engineering sciences* 378, 20180431.
- Holland, T.J.B., Powell, R. (1998). An internally consistent thermodynamic data set for phases of petrological interest. *Journal of Metamorphic Geology* 16, 309–343.
- Holland, T.J.B., Powell, R. (2011) An improved and extended internally consistent thermodynamic dataset for phases of petrological interest, involving a new equation of state for solids. *Journal of Metamorphic Geology* 29, 333–383.
- Iturralde-Vinent, M.A., García-Casco, A., Rojas-Agramonte, Y., Proenza, J.A., Murphy, J.B., Stern, R.J. (2016) The geology of Cuba: A brief overview and synthesis. *GSA Today* 4–10.
- Marchesi, C., Garrido, C.J., Godard, M., Proenza, J.A., Gervilla, F., Blanco-Moreno, J. (2006) Petrogenesis of highly depleted peridotites and gabbroic rocks from the Mayarí-Baracoa Ophiolitic Belt (eastern Cuba). *Contributions to Mineralogy and Petrology* 151, 717–736.
- Pouchou, J.-L., Pichoir, F. (1991) Quantitative Analysis of Homogeneous or Stratified Microvolumes Applying the Model “PAP.” *Electron Probe Quantitation* 31–75.
- Proenza, J., Gervilla, F., Melgarejo, J., Vera, O., Alfonso, P., Fallick, A. (2001) Genesis of sulfide-rich chromite ores by the interaction between chromitite and pegmatitic olivine-norite dikes in the Potosí Mine (Moa-Baracoa ophiolitic massif, Eastern Cuba). *Mineralium Deposita* 36, 658–669.
- Proenza, J., Gervilla, F., Melgarejo, J.C., Bodinier, J.L. (1999) Al- and Cr-rich chromitites from the Mayarí-Baracoa ophiolitic belt (Eastern Cuba): Consequence of interaction between volatile-rich melts and peridotites in suprasubduction mantle. *Economic Geology* 94, 547–566.
- Pujol-Solà, N., Proenza, J.A., García-Casco, A., González-Jiménez, J.M., Román-Alpiste, M.J., Garrido, C.J., Melgarejo, J.C., Gervilla, F., Llovet, X. (2020) Fe-Ti-Zr metasomatism in the oceanic mantle due to extreme differentiation of tholeiitic melts (Moa-Baracoa ophiolite, Cuba). *Lithos* 358–359, 105420.

